Article:
Ross, Jackson L., Gavriloaea, Paul Iulian, Freimuth, Frank et al. (2024) Ultrafast antiferromagnetic switching of Mn2Au with laser-induced optical torques. npj Computational Materials. 234. ISSN: 2057-3960

https://doi.org/10.1038/s41524-024-01416-1

npj | computational materials

Article

Published in partnership with the Shanghai Institute of Ceramics of the Chinese Academy of Sciences

https://doi.org/10.1038/s41524-024-01416-1

Ultrafast antiferromagnetic switching of Mn_2Au with laser-induced optical torques

Jackson L. Ross [1] ✉, Paul-Iulian Gavriloaea [2], Frank Freimuth [3,4], Theodoros Adamantopoulos [4,5], Yuriy Mokrousov [3,4], Richard F. L. Evans [1], Roy Chantrell [1], Rubén M. Otxoa [6,7] & Oksana Chubykalo-Fesenko [2]

Ultrafast manipulation of the Néel vector in metallic antiferromagnets most commonly occurs by generation of spin-orbit (SOT) or spin-transfer (STT) torques. Here, we predict another possibility for antiferromagnetic domain switching by using novel laser optical torques (LOTs). We present results of atomistic spin dynamics simulations from the application of LOTs for all-optical switching of the Néel vector in the antiferromagnet Mn_2Au. The driving mechanism takes advantage of the sizeable exchange enhancement, characteristic of antiferromagnetic dynamics, allowing for picosecond 90 and 180-degree precessional toggle switching of the Néel vector with laser fluences on the order of mJ/cm^2. A special symmetry of these novel torques greatly minimises the over-shooting effect common to precessional spin switching by SOT and STT methods. We demonstrate the opportunity for LOTs to produce deterministic, non-toggle switching of single antiferromagnetic domains. Lastly, we show that even with sizeable ultrafast heating by laser in metallic systems, there exist a large interval of laser parameters where the LOT-assisted toggle and preferential switchings in magnetic grains have probabilities close to one. The proposed protocol could be used on its own for all-optical control of antiferromagnets for computing or memory storage, or in combination with other switching methods to lower energy barriers and/or to prevent over-shooting of the Néel vector.

The potential for fast, deterministic control of the order parameter in metallic antiferromagnets (AFMs) at room-temperature without heavy-metal spin injection is highly promising for spintronics research and device applications. The discovery of classes of high-Néel temperature AFMs, which respond asymmetrically to external stimuli such as Mn_2Au or CuMnAs[1,2], represents an important step for applications in Terahertz (THz) radiation generation[3], as well as for manipulation of magnetic textures for novel AFM spintronics[4]. Their use, however, is restricted to methods which reliably activate those dynamics: the same intrinsic nature which makes AFMs so appealing makes them insensitive to the traditional methods used to control ferromagnetic materials (such as applied fields or microwave excitations).

Currently, the most understood method for controlling the AFM order parameter in spintronic devices is the application of spin orbit torque (SOT)[4–8]. But also of interest is the use of spin transfer torques (STTs)[9–12] and THz excitations to drive AFM switching[13]. However, limitations to these methods provide challenges for practical implementation: SOT control using applied currents requires either precise timing to prevent over-switching[9,14,15], weaker fields for longer duration[16], or repeated short pulses[2,17]. STT driven switching requires complex heterostructures[3,10,15], and over-shooting beyond 90-degrees is still a risk[9,10]. THz driven dynamics represent the most precise method of control, but have not been shown to switch the AFM Néel vector in metals with current experimental THz excitation strength[13]. AFM switching using optical laser pulses has been achieved previously in classes of insulating rare-earth orthoferrites, but only for cryogenic systems due to their low Néel temperatures[18–20]. Thus, it is necessary to look at different materials and switching strategies for room-temperature spintronic applications.

Recent ab initio work[21] has presented a new option for direct manipulation of the order parameter in metallic AFMs: the induction of staggered fields using direct optical laser excitation. The experimental evidence for these torques in metals has been seen in ferromagnetic (FM) materials[12,22], but only recently has the same theoretical formalism[23] been applied to AFMs[24] (and specifically Mn_2Au[21,25]). The frequency dependence of the induced staggered magnetic fields is calculated for optical and THz excitations, and is shown to generate a net non-staggered torque (see Fig. 1).

[1]School of Physics, Engineering and Technology, University of York, York, UK. [2]Instituto de Ciencia de Materiales de Madrid, CSIC, Madrid, Spain. [3]Institute of Physics, Johannes Gutenberg University Mainz, Mainz, Germany. [4]Peter Grünberg Institut and Institute for Advanced Simulation, Forschungszentrum Jülich and JARA, Jülich, Germany. [5]Department of Physics, RWTH Aachen University, Aachen, Germany. [6]Hitachi Cambridge Laboratory, Cambridge, UK. [7]Donostia International Physics Center, Donostia San Sebastian, Spain. ✉e-mail: jackson.ross@york.ac.uk

This torque could potentially switch the AFM order parameter, an idea we consider in detail in the present article.

We present atomistic spin dynamics simulations of an optical frequency excitation from ultrafast laser pulses on Mn_2Au using the coupling scheme suggested in Freimuth et al.[21]. To distinguish between the other laser excitation torques, acting through spin transfer techniques, we call this generated torque a laser optical torque (LOT). Recently, experiments using ultrafast THz pulses have demonstrated induced Mn_2Au dynamics, with modelling predicting the potential for coherent domain switching[13]. Unlike THz pulses, which are predicted to induce both LOT and SOT fields[21], the optical frequency is too far above the AFM frequency to excite SOT dynamics. Note also that the electric field dependence of the generated SOT scales linearly with $\mathbf{E}$[13,21], while the generated LOT scales quadratically with $\mathbf{E}$[21,23,25]. Thus, we focus our work here on demonstrating the possibility to switch the Néel vector in AFM using purely LOTs in optical frequencies. Additionally, we provide a method using the LOT symmetry to preferentially control the switching direction of the Néel vector, allowing for deterministic, non-toggle all-optical switching (AOS) in AFM.

Methods

Atomistic spin dynamics

We perform atomistic spin dynamics simulations in Mn_2Au AFM based on the Landau-Lifshitz-Gilbert (LLG) equation using the open source code VAMPIRE[26] where we included new LOT torques. Unless specified, for the majority of simulations we use a cubic Mn_2Au crystal lattice of 1600 spins, $(3\ \mathrm{nm})^3$. Figure 1 illustrates Mn_2Au unit cell implemented in the atomistic simulations. The effective Heisenberg spin Hamiltonian includes the ferromagnetic (FM) and antiferromagnetic (AFM) exchange interaction terms, two-ion anisotropy mediated by the Au sublayers, fourth-order out-of-plane anisotropy, and the fourth-order rotational in-plane anisotropy (easy axes orientated along the $\langle \pm 110 \rangle$ direction):

$$\mathscr{H} = -\sum_{ij} \mathbf{S}_i \boldsymbol{J}_{ij} \mathbf{S}_j - k_{4\perp} \sum_i \left(S_{i,z}^4 - \tfrac{30}{35} S_{i,z}^2 \right) - k_{4rot} \sum_i \sin^4\theta \cos 4\phi - \mu_s \sum_i \mathbf{S}_i \cdot \mathbf{H}_{LOT,i}. \quad (1)$$

The local magnetic moment directions are given by unit vectors $\mathbf{S}_i$ with length μ_s. θ gives the polar angle of magnetisation, and ϕ the azimuthal angle of magnetisation from the x-coordinate. The magneto-crystalline anisotropies (MCAs) are implemented in Cartesian coordinates using the spherical harmonic formulation given in[27] for accurate four-fold rotational symmetry. Also included is the Au mediated two-ion anisotropy terms, creating a vectorial form of the exchange constants between sites i and j across Au sites such that $\boldsymbol{J}_{ij} = (J_{xx,ij}, J_{yy,ij}, J_{zz,ij} + k_2^{\perp})$[28] (footnote (Simulations of the two-ion anisotropy included as a traditional out-of-plane uniaxial anisotropy show no discernible differences in the phase diagrams, but the two-ion anisotropy is known to have a different temperature scaling[29,30])). Table 1 summarizes the parameters used in the simulations. Shick et al.[28] discussed situations where thin films of Mn_2Au have an additional in-plane, uniaxial strain anisotropy, creating a preferential 180-degree orientation along the $\langle 100 \rangle$ or $\langle 010 \rangle$ directions. While SOTs/STTs have been used to switch 180-degree domains in Mn_2Au[10,14], we confine our simulations to 90-degree domains without the additional in-plane uniaxial anisotropy.

Laser optical torque

Optically-induced torques show strong crystal symmetry and frequency-dependent coupling to the polarised electric field components of the laser. A full analysis of the symmetry requirements in the Mn_2Au bulk crystal was previously presented by Freimuth et al.[21] based on the Keldysh non-equilibrium formalism. There, a linearly or circularly polarised laser pulse was shown to be capable of inducing a torque acting on the Néel vector parameter $\boldsymbol{L}$ via staggered magnetic fields induced by the second-order electric field coupling, which act on the Mn spins in the distinct sublattices of the AFM. The magnitude and spatial symmetry of the predicted torque depend both on the local orientation of the Néel vector $\boldsymbol{L}$, as well as the electric field $\boldsymbol{\epsilon}$ direction of the applied optical pulse. To drive magnetic switching using an in-plane torque, the induced field must be at least equal to the in-plane rotational anisotropy field value of 10.3 mT[14]. Assuming a constant linear relationship between torque and laser intensity, this would require pulses on the order of 2000 mJ/cm^2. Thus, this work seeks to apply out-of-plane torques to take advantage of the exchange enhancement characteristic of antiferromagnetic switching[14,15].

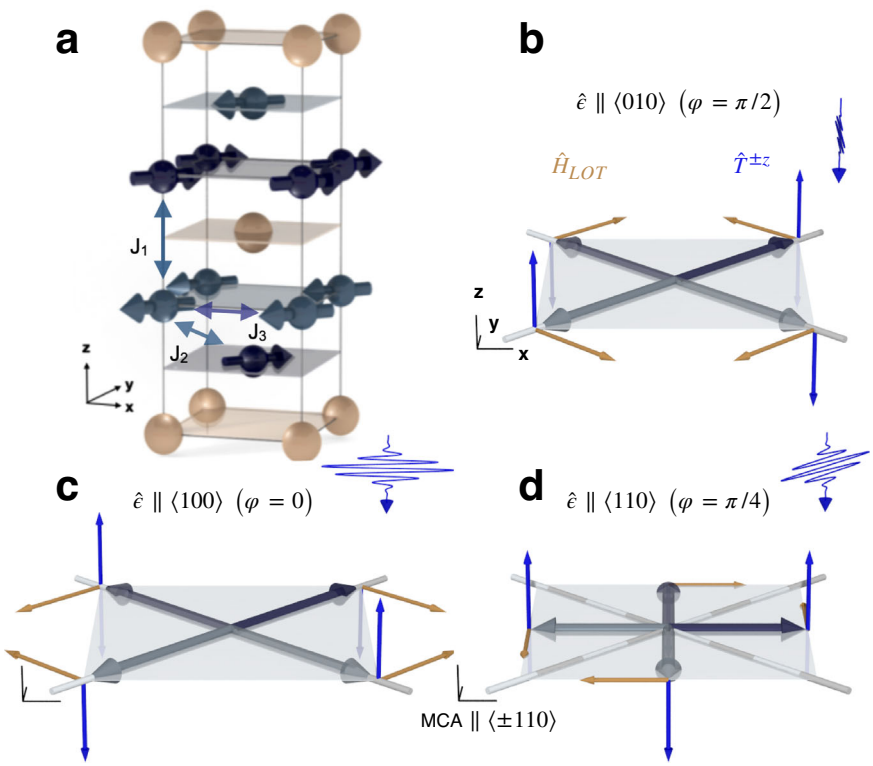

Fig. 1 | Unit cell and diagram of torque symmetry. **a** Unit cell with exchange interactions. **b**–**d** Diagram of net torques from Eq. (3) with light linearly polarised parallel to the azimuthal angle φ from x. Fourth order in-plane magneto-crystalline anisotropy (MCA) along $\langle \pm 110 \rangle$. (Purple): magnetisation vector, (gold): induced field, (blue): resultant torque. **b** electric field polarised along $\langle 010 \rangle$ axis. **c** electric field polarised along $\langle 100 \rangle$ axis (same tensor as in (**b**) but with opposite symmetry). **d** electric field polarised along $\langle 110 \rangle$. **b**,**c** produce equal and opposite torques which are maximal for the easy axes. For consistency we use the polarisation in (**b**) in our simulations.

Table 1 | Exchange and anisotropy constants from Khmelevskyi[45] and Shick et al.[28], in line with experimental values from[33,46] and the lattice constants

Interactions	J_{xx}	J_{yy}	J_{zz}	Unit
J_1	−1.46923	−1.46923	−1.45932	10^{-20} J/link
J_2	−1.09430	−1.09430	−1.08691	10^{-20} J/link
J_3	0.31826	0.31826	0.31826	10^{-20} J/link
	Parameter	**Value**		**Unit**
	μ_s	3.72		μ_B
	$k_{2\perp}$	-1.9727×10^{-22}		J/atom
	$k_{4\perp}$	3.710×10^{-25}		J/atom
	k_{4rot}	1.855×10^{-25}		J/atom
	T_N	1220		K
	a,c	3.328, 8.539		Å

Exchange parameters J_1, J_2, J_3 are defined in Fig. 1a.

The torque tensors[21] depend on the vector components of the electric polarisation and AFM order parameter:

$$\mathscr{T}_i = \frac{a_0^3 I}{c}\left(\frac{\mathscr{E}_H}{\hbar\omega}\right)^2 \mathrm{Im}\sum_{jklm}\chi_{ijklm}\epsilon_j\epsilon_k^* L_l L_m \tag{2}$$

where $a_0 = 4\pi\epsilon_0\hbar^2/(me^2)$ is the Bohr radius, ϵ_0 the vacuum permittivity, $\hbar$ the reduced Plank's constant, m the mass of the free electron, c the speed of light, e the fundamental electron charge, $I = \epsilon_0 c E_0^2/2$ the laser intensity calculated from the electric field component E_0, $\mathscr{E}_H$ the Hartree energy, ϵ_j the jth Cartesian component of the electric field and L_j the jth Cartesian component of the Néel vector, and χ_{ijklm} the corresponding susceptibility components. Importantly, the induced torque sums as the square of the vector components, so the resultant symmetry of the torque can be non-trivial. The Cartesian vector components of $\boldsymbol{\epsilon}$ and $\boldsymbol{L} = (\sin\theta\cos\phi, \sin\theta\sin\phi, \cos\theta)^T$ (we will use φ as the azimuthal angle from x for the laser polarisation and the azimuthal angle of the Néel vector as ϕ). Freimuth et al.[21] present thirty tensors which are allowed by the Mn_2Au orbital symmetry and which produce a torque perpendicular to the Néel vector. Since Mn_2Au has in-plane magnetisation, we disregard tensors corresponding to an out-of-plane Néel vector component to good approximation ($m_z/\mu_B < 10^{-2}$); likewise, since we are interested in exchange enhanced precessional switching, we choose the geometry with the generated torque to be out-of-plane. Lastly, Freimuth et al. find that light incident normal to the AFM plane with electric field linearly polarised parallel to the in-plane angle φ produces the largest torque values. This geometry reduces the set of thirty tensors to two (tensors 4 and 24 in Freimuth et al.). The remaining two tensors calculate an identical magnitude, with the total torque being the sum of each tensor.

In our simulations we vary only the laser intensity and polarisation angle, so we collect other physical and susceptibility constants of Eq. (2) into the variable $\mathscr{T}(I)$ which defines the excitation strength. A linearly polarised pulse with $\boldsymbol{\epsilon}\|\langle 010\rangle$ with intensity $I = 1$ GW/cm^2 set at a photon energy of $h\nu = 1.55$ eV will produce a LOT of magnitude $\mathscr{T} \approx 1.1 \times 10^{-24}$ J, which corresponds to an effective field of 14.5 mT on each magnetic moment (see Fig. 2 in[21]).

Tensor	$\chi_{3\ jklm}$
4	$\langle 32212\rangle - \langle 31112\rangle$
24	$\langle 31211\rangle - \langle 32122\rangle$

The different polarisation and Néel vector dependencies are parameterised according to the Cartesian vector components, such that

$$\begin{aligned}
4 &\equiv \mathscr{T}_3(\langle 32212\rangle - \langle 31112\rangle)\\
&\approx \mathscr{T}_3\left(\sin(\varphi)^2\cos(\phi)\sin(\phi) - \cos(\varphi)^2\cos(\phi)\sin(\phi)\right)\\
&= -\tfrac{\mathscr{T}_3}{2}\cos(2\varphi)\sin(2\phi)\\
24 &\equiv \mathscr{T}_3(\langle 31211\rangle - \langle 32122\rangle)\\
&\approx \mathscr{T}_3\left(\sin(\varphi)\cos(\varphi)\cos(\phi)^2 - \sin(\varphi)\cos(\varphi)\sin(\phi)^2\right)\\
&= -\tfrac{\mathscr{T}_3}{2}\sin(2\varphi)\cos(2\phi)\\
4 + 24 &\approx \tfrac{\mathscr{T}_3}{2}\sin(2\varphi - 2\phi).
\end{aligned}$$

For comparison, we can also consider a sub-optimal switching polarisation geometry with the laser polarisation rotated further along the polar angle: an electric field polarisation along $\langle 101\rangle$, photon energy of 1.55 eV, intensity of 10 GW/cm^2, and Néel vector along $\langle 100\rangle$ produces an *in-plane* torque on each magnetic site of $\approx 10^{-24}$ J ($H_{LOT} = 0.05$ mT)[21]. The Keyldish formalism in[21,23] uses a constant broadening parameter Γ to simulate disorder and finite lifetimes. A $\Gamma = 25$ meV approximates a clean metallic sample at room temperature, though recent experiments suggest the Γ value for Mn_2Au may in fact be lower[13], leading to a larger torque constant. This value takes into account the non-equilibrium disorder from the laser excitation, so we hold it constant during the simulation.

The polarisation (φ) and Néel angle (ϕ) dependent torque are thus parameterised as an effective field acting always perpendicular to the spin direction, as:

$$\mathbf{H}_{\mathrm{LOT}} = \frac{1}{\mu_s}\tilde{\mathscr{T}}(t)\sin(2\varphi - 2\phi)\hat{z}\times\mathbf{S} \tag{3}$$

Eq. (2) provides a linear relationship with laser intensity. Thus, to simulate the influence of the LOT generated by an ultrafast laser pulse, we scale the laser intensity following a Gaussian time-dependent profile, with the pulse duration t_p giving the time at full-width at half-height of the pulse intensity[31] as

$$\tilde{\mathscr{T}}(t) = \mathscr{T}(I)\exp\left\{-4\ln 2\left(\frac{t - 1.5t_p}{t_p}\right)^2\right\}, \tag{4}$$

The directions of the induced fields for various light polarisation angles are illustrated in Fig. 1. The staggered fields then lead to a non-staggered effective torque. Figure 1b,c shows the laser polarisation directions corresponding with the maximal torques useful for switching. Figure 1d shows the light polarisation along $\langle 110\rangle$ inducing a torque relationship which does not produce a torque useful for switching, as the maximal torque generated is when the Néel vector is along the hard axis. Thus, in the following simulations we use linearly polarised light with polarization parallel to $\langle 010\rangle$ (Fig. 1b). The case of Fig. 1c produces the torque with the opposite direction and the same magnitude.

Results

Toggle switching

The LOT modelled by Eq. (3) produces 90, 180, and 270-degree precessional switching of the Néel vector in Mn_2Au by *exchange enhancement* generated by the out-of-plane canting as also seen in simulations of the SOT switching[14,32]. Figure 2 provides example of sublattice magnetisation traces for 90 (grey and blue) and 180-degree (gold) switching. The initial laser induced field causes an out-of-plane canting of the magnetisation, generating a large non-staggered torque on the magnetisation sublattices to rotate the Néel vector.

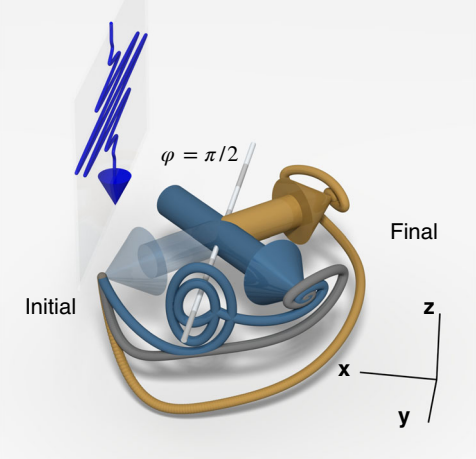

Fig. 2 | Diagram of example magnetisation vector during switching. Sublattice magnetisation vectors switching from ⟨110⟩ to ⟨ −110⟩ with $\boldsymbol{\epsilon} \parallel \langle 010 \rangle$. (Opaque): initial orientation. (Bar): precession axis. (grey): $t_p = 400$ fs, $I = 2$ GW/cm^2, (gold): $t_p = 400$ fs, $I = 4$ GW/cm^2, and (blue): $t_p = 3$ ps, $I = 5$ GW/cm^2 (z magnetisation scaled 100× for visibility).

We model the action of the LOT using four sequential pulses 400 fs long and 8 ps apart for laser intensities $I = 2$ GW/cm^2 ($H_{max} = 42$ mT; blue) and $I = 4$ GW/cm^2 ($H_{max} = 84$ mT; gold). Each consequent pulse produces switching, as shown in Fig. 3. Note the absence of the L_z component; i.e. the Néel vector is rotated in-plane as also typical for the SOT switching[13]. Unlike the SOT considered in[14,16], the LOT has the additional feature of changing sign during the switching: the intrinsic spatial symmetry defined in Eq. (3) ensures the induced LOT changes its sign for any 90-degree rotation of the Néel vector. This allows for both clockwise and counter-clockwise switching by means of the same laser polarisation, i.e. *toggle switching* (see Fig. 3). In contrast is the SOT torque, where the direction of the applied current needs to be constantly inverted to change the handedness of rotation for 90-degree switching[2,13].

180-degree switching is possible with LOT for the same laser polarisation used to generate 90-degree switching, but with strong enough intensities capable to induce larger out-of-plane canting, providing more exchange enhanced torque for the Néel vector rotation (compare the magnitude of the torques in (b) and magnetisation in (d) of Fig. 3). The 180-degree switching events are in the same direction, consistently inducing an out-of-plane magnetisation with the same sign. We believe that the differences in magnitude and sign during the 90 and 180-degree switching events could be externally detected using a careful experimental setup.

Figure 4 presents the switching phase diagrams as a function of laser intensity and duration for two Gilbert damping parameters $\alpha = 0.001$ and $\alpha = 0.01$. The colour variation shows intervals of 90-degree switching, typical for precessional switching. Importantly, the switching can be produced by ultrafast laser pulses of several picosecond duration and even below. The absorbed fluence of the sample is approximately linear with intensity and pulse duration[23,25]. Remarkably, we observe an absorbed fluence of 0.5 mJ/cm^2 ($I = 0.3$ GW/cm^2, $H_{crit} = 6.34$ mT) is sufficient to induce switching on the sub-picosecond timescale for the smaller damping value of $\alpha = 0.001$. Increasing the damping parameter shows a linear dependence in the critical field (see Fig. 4b), commensurate with the theory of SOT switching[16].

Analytically, the dynamic behaviour of collinear AFMs under staggered in-plane SOT fields is discussed in[14]. Here, the critical field (H_{crit}) for switching has been shown to depend on the characteristic exchange, anisotropy, and induced magnetic fields. Following the method of[14]—modified for the LOT induced field—the dynamics of the Néel vector in the xy plane can be describ ed by the following equation:

$$\ddot{\phi} + \frac{\omega_R^2}{4}\cos 4\phi - \gamma\omega_e \frac{\mathscr{T}(I)}{\mu_s}\sin(2\varphi - 2\phi) + 2\alpha\omega_e\dot{\phi} = 0 \qquad (5)$$

where $\omega_e = |5(J_1 + 4J_2)|\gamma/\mu_s$ is the AFM exchange frequency (ignoring the 2-ion anisotropy term to good approximation), $\omega_{4\|} = 2\gamma k_{4rot}$ is the fourth order in-plane anisotropy frequency, α is the atomistic damping parameter, γ is the gyromagnetic ratio, and $\omega_R = \sqrt{2\omega_e\omega_{4\|}}$. The parameter $\mathscr{T}(I)/\mu_s$ corresponds to the amplitude of the LOT field. If the Néel vector is only considered in the interval of its azimuthal angle $\phi \in [0, \pi/4]$, the critical field for the switching for infinitely long pulse lengths is $H_{crit} = \omega_{4\|}/(2\gamma)$: a factor of 2 larger than for SOT[14,16], due to the sin 2ϕ dependence of the LOT field. Analytically, our constants predict an $H_{crit} = 5.16$ mT, matching well with our simulations for $\alpha = 0.001$ (see horizontal line in Fig. 4a).

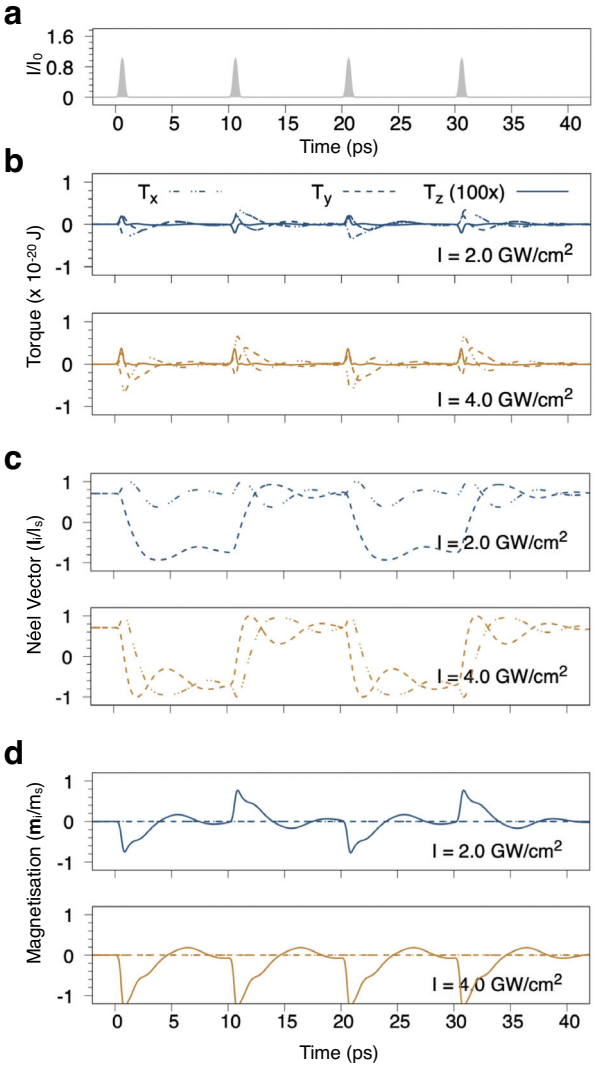

Fig. 3 | Toggle switching of the Néel vector with multiple optical pulses. a laser intensity of the pulse (400 fs) 8 ps apart. **b** total torque. Note that the T_z has been scaled 100x for visibility. (dashed): T_x; (dot-dashed): T_y; (solid): T_z. **c** x and y Néel vector components $\boldsymbol{L}_i = (\boldsymbol{m}_1 - \boldsymbol{m}_2)/2$. $L_s = |L|$. (dashed): L_x; (dot-dashed): L_y. **d** Net magnetisation $\boldsymbol{m}_i = (\boldsymbol{m}_1 + \boldsymbol{m}_2)/2$. $m_s = |m|$. (dashed): $m_x = m_y$; (dash-dot): m_z (scaled 200× for visibility). Blue lines show 90-degree toggle switching for four sequential pulses. Gold shows 180-degree toggle switching for four sequential pulses.

For short pulse lengths the critical switching field can be evaluated as

$$\frac{H_{crit}}{H_{crit}(\tau \to \infty)} = \coth\left(\frac{2t_p}{\tau_e\sqrt{2\pi}}\frac{\omega_R}{\omega_e}\right), \tag{6}$$

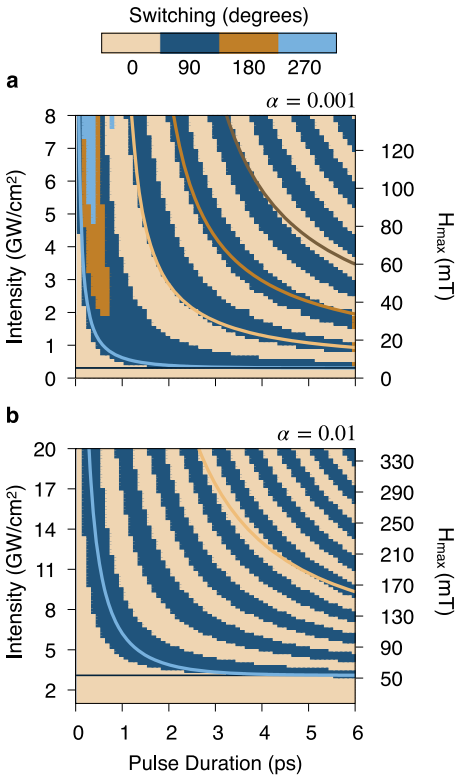

Fig. 4 | Switching phase diagram in terms of laser intensity and duration. Colours represent the end change of angle from ⟨110⟩. The corresponding maximum field strength for the laser intensity is given on the second y-axis. Solid colour lines show the analytic H_{crit} values from Eq. (7) **a** for $\alpha = 0.001$. Black line: $H_{crit} = \omega_{4\|}/(2\gamma) = 5.16$ mT. **b** $\alpha = 0.01$ Black line: $10\times H_{crit}$, showing that the critical field scales linearly with damping parameter.

where $\tau_e \approx \pi/(2\omega_e)$ is the timescale of the exchange interaction (characteristic precessional time for the Néel vector for rotation over 90-degrees), which is then scaled in Eq. (6) by $\sqrt{2\pi}/2$ to account for the Gaussian profile of the laser pulse. Then, τ_p can be called the characteristic pulse duration $\tau_p = 2\tau_e\omega_e/\omega_R$ such that $\coth(2) \approx 1$, necessary to achieve energy-efficient switching with a minimum LOT.

Importantly, only for high intensities and short pulse duration is the inertia generated by the exchange torque susceptible to overshooting, either by 180-degrees or even 270-degrees (orange and light blue colour in Fig. 4). Qualitatively, this is illustrated by the gold track in Fig. 2 For pulse lengths beyond 1 ps: rather than continually driving the precessional switching using exchange enhancement, the long pulse duration has the Néel vector precessing along the laser polarisation axis (blue curve in Fig. 2). The timing of these precessions follows the characteristic exchange period, and can be modelled by modifying Eq. (6) to take into account the additional precessions around the LOT polarisation vector: for n precessions, the minimum pulse time to switch the Néel vector at high intensity is proportional to the exchange precession timescale and precession number, $4n\tau_e\sqrt{2\pi}$. This gives a rough approximation to the critical field and laser pulse time:

$$H_{crit}(\tau, n) = nH_{crit}^{\tau\to\infty}\coth\left(\frac{2t_p\omega_R}{n\tau_e\sqrt{2\pi}\omega_e} - \frac{4n\tau_e\sqrt{2\pi}}{t_p}\right) \tag{7}$$

The analytical estimates of fields and pulse durations are presented in Fig. 4a), showing a good agreement for $n \le 3$ with the lowest damping value, especially considering the approximations made. Since the precession frequency of these excitations are determined by the exchange and anisotropy values, it represents an activation of the in-plane AFM THz mode–an unusual opportunity to activate a THz mode using optical excitation. Importantly, this represents an opportunity for all optical toggle switching where the driving mechanism is predicted to be induced fields, rather than thermal activation (see Temprature effects in Results).

Preferential switching

Equation (2) shows that the quadratic reliance on the electric field polarisation of the generated torque in Eq. (3) allows a shift of the maximum torque away from the easy axis by rotation of the laser polarisation vector. Contrary to the toggle switching caused by $\boldsymbol{\epsilon}\|\langle 100\rangle$ or ⟨010⟩ displayed in Fig. 3, shifting the azimuthal angle of the laser polarisation will create an asymmetric torque profile, influencing the

Fig. 5 | Diagram of torque symmetry for rotated laser polarisation. (Dark blue line): relative size and direction of the out-of-plane torque as a function of the magnetisation direction for electric field polarisation $\boldsymbol{\epsilon} \| 5\pi/8$. Opaque shows comparable torque and field sizes further along the path of motion from the easy axis. Note the unequal torque generated between clockwise and counter-clockwise motion. (Faded blue line): the same for $\boldsymbol{\epsilon} \| \pi/2$. Gold vectors denote relative field size and direction.

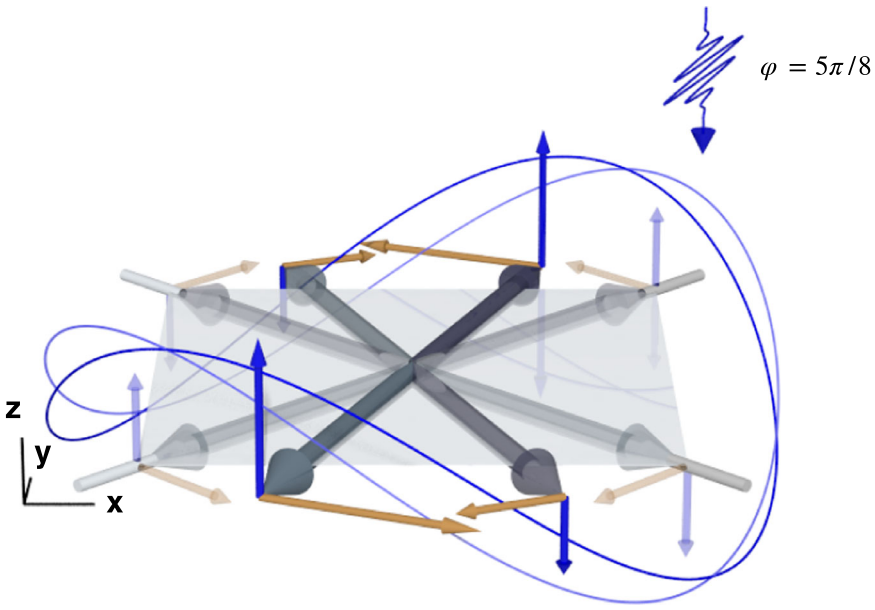

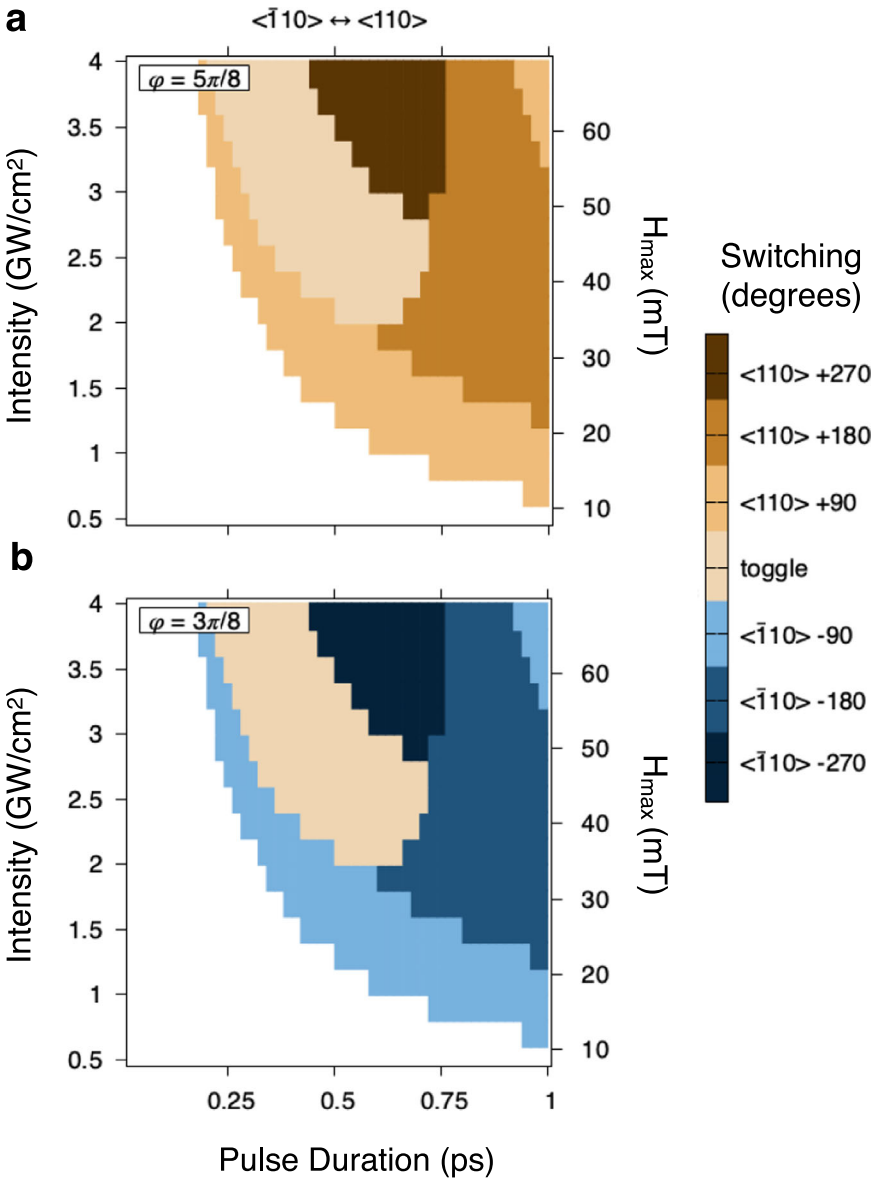

Fig. 6 | Switching phase diagram for rotated laser polarisations. a $\varphi = 5\pi/8$ and **b** $\varphi = 3\pi/8$ showing preferential (**a**) right-handed switching for starting magnetisation vector orientation $\langle 110 \rangle$ vs (**b**) preferential left-handed switching for starting orientations $\langle \bar{1}10 \rangle$.

Néel vector dynamical path from the four easy axes (see Fig. 5). Thus, the magnetisation will experience a larger torque when starting from only two of the four easy axis directions, giving a preference between clockwise and counter-clockwise switching (Fig. 5). This breaks the four-fold degenerate easy axes into "large" and "small" generated torques.

Figure 6 shows the phase diagram of laser pulse intensity and duration which distinguishes between non-toggle (preferential) switching and toggle switching for starting orientations $\langle 110 \rangle$ and $\langle \bar{1}10 \rangle$ for laser polarisations $\varphi = 3\pi/8$ (Fig. 6a) and $\varphi = 5\pi/8$ (Fig. 6b). The switching area labelled "toggle" switching in Fig. 6 is the region where both starting orientations switch either 90 or 180 degrees. Furthermore, Fig. 6a) has preferential right-handed switching for the $\langle 110 \rangle$ orientation at low fluence, with toggle switching for both orientations at higher fluence and middling pulse duration. A 45-degree rotation of the laser polarisation changes the sign of the preferential torque, making left-handed switching from $\langle \bar{1}10 \rangle$ easier at low fluence (Fig. 6b). Either laser orientation can be used to preferentially write the Néel vector to a desired orientation without changing the polarisation angle by using variable pulse duration/intensity (as shown in the next section).

Deterministic control of the Néel vector

The anisotropic magneto-resistance (AMR) measurements typically used to determine the magnetic state in antiferromagnets[2] depend only on the parallel component of the Néel vector "aligned" or "anti-aligned" with the resistance measurement vector. Thus, the $\pi/4$ and $3\pi/4$ ($-\pi/4$ and $-3\pi/4$) Néel states can be considered equivalent starting orientations for AMR measurements. This reduction from 4-fold to 2-fold symmetry allows the possibility to deterministically switch between non-equivalent orientations.

The preference for rotation direction from the starting orientation can be used in combination with the toggle switching (achieved by the same laser polarisation but with more intense pulses) to deterministically control the Néel vector for the two non-equivalent directions. To demonstrate how preferential and toggle switching pulses from the same laser polarisation could be used for this purpose, we simulate a series of four laser pulses of varying intensity for each of the four starting orientations.

Figure 7 details the Néel vector dynamics following sequential laser pulses with starting AFM order parameters along each of the easy axes with laser polarisation parallel to the $5\pi/8$ azimuthal angle. The pulses are separated by 16 ps to allow the magnetisation to return to equilibrium. The second pulse has more intensity than the others (Fig. 7a). Figure 7b shows that the first, "small" pulse failed to switch the $3\pi/4$ and $-\pi/4$ orientations,

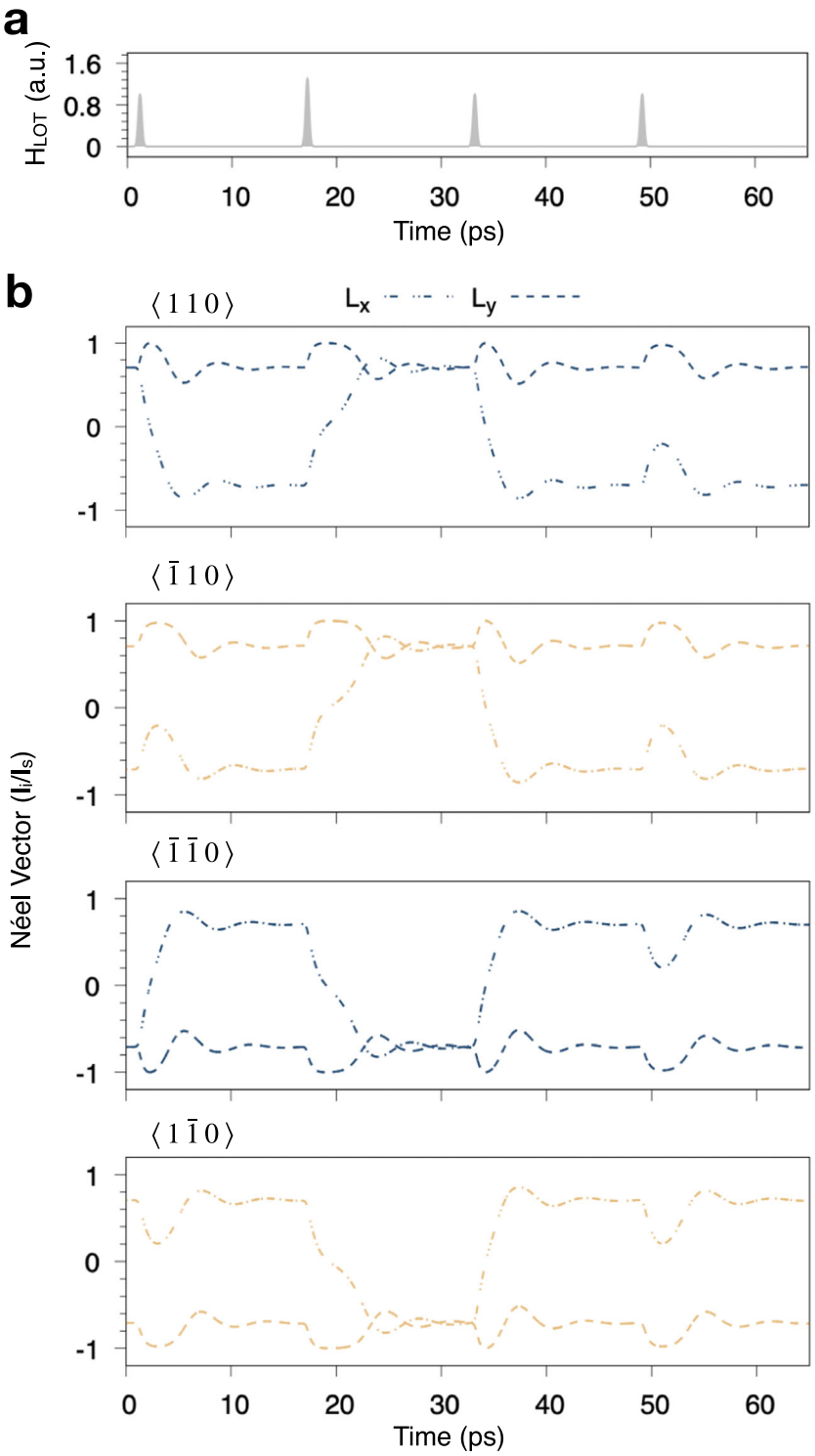

Fig. 7 | Dynamics of the Néel order parameter for laser excitation. Four sequential pulses of 400 fs width and 16 ps apart. Each panel shows the Néel vector starting along each easy axis. The second pulse has an intensity of 2.6 GW/cm^2; all others are 2 GW/cm^2. Light polarisation is parallel to the angle $\varphi = 5\pi/8$. **a** Normalised laser intensity. **b** Néel vector with time.

but switching took place with the second, "large" pulse. Now that the magnetisation has been reoriented to the quadrant which experiences the maximal torque, it does successfully switch following a small pulse. This dependence is shown with the $\pi/4$ and $-3\pi/4$ orientations as well: since they start their magnetisation in the maximal torque quadrant, they show switching following the first, "small" pulse, as well as the second and third pulses, but not the fourth, since the magnetisation has moved to a minimum torque quadrant. Thus, the equivalent $\langle 110 \rangle$ ($\pi/4$) and $\langle \bar{1}\bar{1}0 \rangle$ ($3\pi/4$) states both switch to the other non-equivalent direction, defined by either $\langle 1\bar{1}0 \rangle$ ($-3\pi/4$) or $\langle 1\bar{1}0 \rangle$ ($-\pi/4$). The same is also true for the other pair of the equivalent orientations. Most importantly, by choosing the appropriate combination of pulses, we can fully control the switching, or lack of, to one of the non-equivalent orientations.

Temperature effects

While the predicted laser intensities necessary for switching are quite low, an ultrafast temperature raise can be expected in this material, especially due to a high conductivity of Au in metallic Mn_2Au. Our low temperature results, however, could be applicable to insulating AFMs with low Néel temperatures. The electron and phonon temperature dynamics for some typical laser

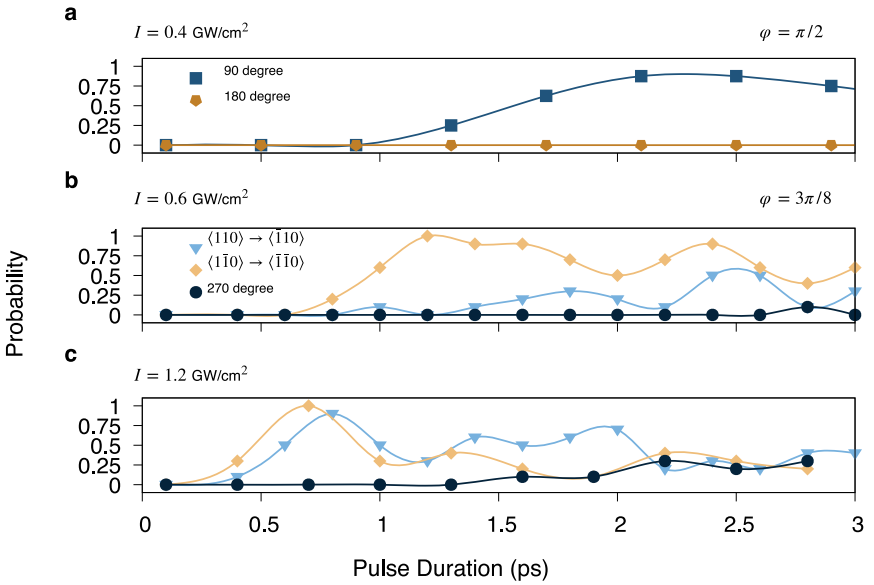

Fig. 8 | Temperature-dependent switching probability. a Switching probability for a grain $75 \times 75 \times 10$ nm^3 with laser polarisation along $\varphi = \pi/2$. Laser intensity $I = 0.4$ GW/cm^2. Unpolarised (thermal-only) laser pulses show no switching probability. **b** Laser intensity $I = 0.6$ GW/cm^2. Probability of switching depending on starting orientation. Laser polarisation along $\varphi = 3\pi/8$. **c** Laser intensity $I = 1.2$ GW/cm^2.

intensities/durations is presented in the Supplementary Information I. In what follows, we couple our atomistic simulations to the electronic temperature given by the two-temperature model (see details in Supplementary Information I).

A full analysis of temperature effects on LOT switching is beyond the scope of this article and would require a very large system size and large statistics. Here we model a granular Mn_2Au system, similar to the one experimentally studied in[13,33,34]. As seen in other temperature switching models[16,24,32], the inclusion of temperature lowers the anisotropy barrier for switching and introduces the superparamagnetic effect, which is system-size dependent. We model a magnetic grain of approximately ($75 \times 75 \times 10$ nm^3) and calculate the switching probability for this grain. As seen in Fig. 8a, in the absence of LOT and the presence of laser heating, this system does not praesent the superparamagnetic effect. Moreover, the transient heating from the laser pulse for intensities we consider is not enough to fully quench the magnetisation, and successive pulses do not raise the lattice temperature of the system substantially, which could potentially damage the sample.

In the presence of LOT, the results in Fig. 8a show the toggle switching with the probability approaching one in a range of pulse durations for a given intensity and $\varphi = \pi/2$ polarisation. Figure 8b shows the right-handed vs left-handed switching probabilities for a rotated $\varphi = 3\pi/8$ laser orientation on different Néel vector starting orientations with intensity $I = 0.6$ GW/cm^2, Fig. 8c) intensity $I = 1.2$ GW/cm^2. The lower pulse intensity shows the clear preference for the $\langle 1\bar{1}0 \rangle$ starting orientation, while a larger intensity with shorter pulse duration provides toggle switching with high probability for both orientations. A longer laser pulse shows saturation of the probability, consistent with stochastic switching from thermal activation. Therefore, while the addition of temperature to the simulations lowers the energy barrier for the system to achieve toggle switching, the simulated magnetic grain shows all types of dynamics discussed previously. We expect the temperature effects to be even smaller for larger system sizes.

Discussion

By means of atomistic spin dynamics simulations with LOT we predict the possibility for metallic AFM all optical switching (AOS) on the sub- and low picosecond timescale. The unique symmetry relations of this torque prioritise 90-degree toggle switching for long pulse times, but also allow 180 or 270-degree switching provided sufficiently large pulse intensities are used. Importantly, repeated laser pulses do not drive the order parameter continuously clockwise (counter-clockwise) like SOT/STT excitations, but instead provides toggle switching to the Néel vector. We also predict that rotation of the laser polarisation to generate a quadrant-asymmetric torque introduces an additional level of control to the switching process, allowing for preferential, non-toggle switching. Finally, the combination of toggle and non-toggle switching can provide a full control over the two-fold Néel vector non-equivalent orientations, distinguishable in the AMR measurements. Temperature simulations which include the effects of laser heating on the granular metallic sample show results consistent with the 0 K diagrams. These results suggest the significant opportunity the LOT could provide for deterministic AOS in AFM spintronics.

The efficiency of the LOT may be preferred to other AOS methods. The minimum pulse intensity and fluence necessary to switch on the low sub-picosecond timescale using the LOT is estimated 1 GW/cm^2 and 0.65 mJ/cm^2, respectively. This is compared to the fluence for GdFeCo AOS in[35] of 4.4 mJ/cm^2 and the 6.51 mJ/cm^2 for Fe ultrafast demagnetisation generating spin current which is used for the STT switching in[10]. Additionally, the LOT has the advantage of not needing to be applied over short fs time scales to outpace the large laser heating effect from large intensities[24].

The category of the torque as an optical-frequency excitation also has direct implications for ease of experimental procedure: the generation of THz frequencies is a non-trivial procedure, and metallic AFM switching using THz excitation remains hampered by insufficient effective electric fields[13]. The LOT may thus offer a more accessible route to activating THz AFM modes for room-temperature spintronic devices, even with the large frequency discrepancy between the laser pulse and AFM mode. This application could be extended to Mn_2Au heterostructure systems with exchange bias or multi-domain systems used for neuromorphic computing[36] where THz activation through current or STT is less-preferable.

Applications of this torque method could be done in place of (or in conjunction with) spin-injected SOT/STT and intrinsic SOT control methods to improve the efficiency of switching[14], domain wall driving[37–40], or THz generation[41–43]. Moreover, this work seeks to expand the efficacy of second order laser coupling schemes for AFMs: while the results presented here are specifically for Mn_2Au, we extend the comment in Freimuth et al. that LOT is not unique to Mn_2Au[21]; second order terms in electric field with exotic and useful symmetries could exist in many other PT-symmetric AFMs, undiscovered and unlooked for up to now. While the effects of second order optical coupling has been used to switch insulating AFMs at cryogenic temperatures[20,44], their effects have not been studied for metallic AFMs. As the study and characterisation of asymmetric AFM responses to

external stimuli continues, more materials of relevant symmetry should be included in the theoretical and experimental study of optically generated spin torques beyond the first order coupling traditionally explored for metallic magnetic materials.

Data availability

The data that support the findings of this study are available from the corresponding author upon reasonable request.

Received: 9 January 2024; Accepted: 3 September 2024;
Published online: 03 October 2024

References

1. Wadley, P. et al. Electrical switching of an antiferromagnet. *Science* **351**, 587–590 (2016).
2. Bodnar, S. Y. et al. Writing and reading antiferromagnetic mn2au by néel spin-orbit torques and large anisotropic magnetoresistance. *Nat. Commun.* **9**, 348 (2018).
3. Ni, Y. et al. Temperature-dependent terahertz emission from co/mn2au spintronic bilayers. *physica status solidi(RRL).* **15**, https://doi.org/10.1002/pssr.202100290 (2021).
4. Baltz, V. et al. Antiferromagnetic spintronics. *Rev. Mod. Phys.* **90**, 015005 (2018).
5. Jungwirth, T., Marti, X., Wadley, P. & Wunderlich, J. Antiferromagnetic spintronics. *Nat. Nanotechnol.* **11**, 231–241 (2016).
6. Jia, X.-T. et al. Spin hall effect induced néel order switching in the tetragonal mn2au. *J. Phys. D: Appl. Phys.* **53**, 245001 (2020).
7. Zhou, X. et al. From fieldlike torque to antidamping torque in antiferromagnetic mn_2au. *Phys. Rev. Appl.* **11**, https://doi.org/10.1103/PhysRevApplied.11.054030 (2019).
8. Godinho, J. et al. Electrically induced and detected néel vector reversal in a collinear antiferromagnet. *Nat. Commun.* **9**, 4686 (2018).
9. Cheng, R., Daniels, M. W., Zhu, J.-G. & Xiao, D. Ultrafast switching of antiferromagnets via spin-transfer torque. *Phys. Rev. B* **91**, 064423 (2015).
10. Weißenhofer, M., Foggetti, F., Nowak, U. & Oppeneer, P. M. Néel vector switching and terahertz spin-wave excitation in due to femtosecond spin-transfer torques. *Phys. Rev. B* **107**, https://doi.org/10.1103/physrevb.107.174424 (2023).
11. Huang, L. et al. Antiferromagnetic inverse spin hall effect. *Adv. Mater.* **34**, https://doi.org/10.1002/adma.202205988 (2022).
12. Němec, P. et al. Experimental observation of the optical spin transfer torque. *Nat. Phys.* **8**, 411–415 (2012).
13. Behovits, Y. et al. Terahertz néel spin-orbit torques drive nonlinear magnon dynamics in antiferromagnetic mn2au. *Nat. Commun.* **14**, https://doi.org/10.1038/s41467-023-41569-z (2023).
14. Roy, P. E., Otxoa, R. M. & Wunderlich, J. Robust picosecond writing of a layered antiferromagnet by staggered spin-orbit fields. *Phys. Rev. B* **94**, https://doi.org/10.1103/physrevb.94.014439 (2016).
15. Gomonay, H. V. & Loktev, V. M. Spin transfer and current-induced switching in antiferromagnets. *Phys. Rev. B* **81**, 144427 (2010).
16. Rama-Eiroa, R., Otxoa, R. M. & Atxitia, U. Temperature-dependent critical spin-orbit field for orthogonal switching in antiferromagnets. *Appl. Phys. Lett.* **121**, 132401 (2022).
17. Olejník, K. et al. Terahertz electrical writing speed in an antiferromagnetic memory. *Sci. Adv.* **4**, eaar3566 (2018).
18. Kimel, A. V. et al. Ultrafast non-thermal control of magnetization by instantaneous photomagnetic pulses. *Nature* **435**, 655–657 (2005).
19. Kimel, A. V. et al. Inertia-driven spin switching in antiferromagnets. *Nat. Phys.* **5**, 727–731 (2009).
20. de Jong, J. A. et al. Coherent control of the route of an ultrafast magnetic phase transition via low-amplitude spin precession. *Phys. Rev. Lett.* **108**, https://doi.org/10.1103/PhysRevLett.108.157601 (2012).
21. Freimuth, F., Blügel, S. & Mokrousov, Y. Laser-induced torques in metallic antiferromagnets. *Phys. Rev. B* **103**, https://doi.org/10.1103/physrevb.103.174429 (2021).
22. Choi, G.-M., Schleife, A. & Cahill, D. G. Optical-helicity-driven magnetization dynamics in metallic ferromagnets. *Nat. Commun.* **8**, https://doi.org/10.1038/ncomms15085 (2017).
23. Freimuth, F., Blügel, S. & Mokrousov, Y. Laser-induced torques in metallic ferromagnets. *Phys. Rev. B* **94**, https://doi.org/10.1103/physrevb.94.144432 (2016).
24. Dannegger, T. et al. Ultrafast coherent all-optical switching of an antiferromagnet with the inverse faraday effect. *Phys. Rev. B* **104**, https://doi.org/10.1103/PhysRevB.104.L060413 (2021).
25. Merte, M. et al. Photocurrents, inverse faraday effect, and photospin hall effect in mn2au. *APL Mater.* **11**, https://doi.org/10.1063/5.0149955 (2023).
26. Evans, R. F. L. et al. Atomistic spin model simulations of magnetic nanomaterials. *J. Phys. Condens. Matter* **26**, 103202 (2014).
27. Collings, J. B., Rama-Eiroa, R., Otxoa, R. M., Evans, R. F. L. & Chantrell, R. W. Generalized form of the magnetic anisotropy field in micromagnetic and atomistic spin models. *Phys. Rev. B* **107**, 064413 (2023).
28. Shick, A. B., Khmelevskyi, S., Mryasov, O. N., Wunderlich, J. & Jungwirth, T. Spin-orbit coupling induced anisotropy effects in bimetallic antiferromagnets: A route towards antiferromagnetic spintronics. *Phys. Rev. B* **81**, 212409 (2010).
29. Rózsa, L. & Atxitia, U. Temperature dependence of spin-model parameters in antiferromagnets. *Phys. Rev. Res.* **5**, https://doi.org/10.1103/PhysRevResearch.5.023139 (2023).
30. Evans, R. F. L., Rózsa, L., Jenkins, S. & Atxitia, U. Temperature scaling of two-ion anisotropy in pure and mixed anisotropy systems. *Phys. Rev. B* **102**, 020412 (2020).
31. Jiang, L. & Tsai, H.-L. Improved two-temperature model and its application in ultrashort laser heating of metal films. *J. Heat. Transf.* **127**, 1167–1173 (2005).
32. Selzer, S. et al. Current-induced switching of antiferromagnetic order in antiferromagnetics from first principles. *Phys. Rev. B* **105**, https://doi.org/10.1103/physrevb.105.174416 (2022).
33. Sapozhnik, A. A. et al. Direct imaging of antiferromagnetic domains in mn_2au manipulated by high magnetic fields. *Phys. Rev. B* **97**, https://doi.org/10.1103/PhysRevB.97.134429 (2018).
34. Bodnar, S. et al. Imaging of current induced néel vector switching in antiferromagnetic mn2au. *Phys. Rev. B* **99**, https://doi.org/10.1103/PhysRevB.99.140409 (2019).
35. Radu, I. et al. Transient ferromagnetic-like state mediating ultrafast reversal of antiferromagnetically coupled spins. *Nature* **472**, 205–208 (2011).
36. Kurenkov, A., Fukami, S. & Ohno, H. Neuromorphic computing with antiferromagnetic spintronics. *J. Appl. Phys.* **128**, https://doi.org/10.1063/5.0009482 (2020).
37. Otxoa, R. M., Atxitia, U., Roy, P. E. & Chubykalo-Fesenko, O. Giant localised spin-peltier effect due to ultrafast domain wall motion in antiferromagnetic metals. *Commun. Phys.* **3**, https://doi.org/10.1038/s42005-020-0296-4 (2020).
38. Otxoa, R. M. et al. Topologically-mediated energy release by relativistic antiferromagnetic solitons. *Phys. Rev. Res.* **3**, 043069 (2021).
39. Rama-Eiroa, R. et al. Inertial domain wall characterization in layered multisublattice antiferromagnets. *J. Magn. Magn. Mater.* **560**, 169566 (2022).
40. Otxoa, R. M., Tatara, G., Roy, P. E. & Chubykalo-Fesenko, O. Tailoring elastic and inelastic collisions of relativistic antiferromagnetic domain walls. *Sci. Rep.* **13**, 21153 (2023).
41. Kalashnikova, A. M. et al. Impulsive generation of coherent magnons by linearly polarized light in the easy-plane antiferromagnets. *Phys. Rev. Lett.* **99**, https://doi.org/10.1103/PhysRevLett.99.167205 (2007).
42. Satoh, T. et al. Spin oscillations in antiferromagnetic nio triggered by circularly polarized light. *Phys. Rev. Lett.* **105**, https://doi.org/10.1103/PhysRevLett.105.077402 (2010).

43. Tatara, G., Akosa, C. A. & Otxoa de Zuazola, R. M. Magnon pair emission from a relativistic domain wall in antiferromagnets. *Phys. Rev. Res.* **2**, 043226 (2020).
44. Afanasiev, D. et al. Control of the ultrafast photoinduced magnetization across the morin transition in dyfeo3. *Phys. Rev. Lett.* **116**, https://doi.org/10.1103/PhysRevLett.116.097401 (2016).
45. Khmelevskyi, S. & Mohn, P. Layered antiferromagnetism with high neel temperature in the intermetallic compound mn2au. *Appl. Phys. Lett.* **93**, 162503 (2008).
46. Barthem, V., Colin, C., Mayaffre, H., Julien, M.-H. & Givord, D. Revealing the properties of mn2au for antiferromagnetic spintronics. *Nat. Commun.* **4**, https://doi.org/10.1038/ncomms3892 (2013).

Acknowledgements

The authors acknowledge funding from the European Union's Horizon 2020 research and innovation programme under the Marie Skłodowska-Curie International Training Network COMRAD (grant agreement No 861300). The atomistic simulations were undertaken on the VIKING cluster, which is a high performance compute facility provided by the University of York. F.F. and Y.M. acknowledge the funding by the Deutsche Forschungsgemeinschaft (DFG, German Research Foundation) – TRR 173/2 – 268565370 (project A11) and Sino-German research project DISTOMAT (MO 1731/10-1) of the DFG. The work of O.C.-F. has been supported by DFG via CRC/TRR 227, project ID 328545488 (Project MF).

Author contributions

J.L.R., R.F.L.E., R.C., O.CF., and R.M.O. conceived the experiment. Y.M., F.F., and T.A. provided the ab initio data, symmetry, and theory. J.L.R. developed the basis of the theoretical model, performed the simulations, and wrote the original draft. PJ.G. and R.M.O. supported the theoretical model. PJ.G. contributed to the original draft. O.CF. lead the draft editing. All authors reviewed and commented on the paper.

Competing interests

The authors declare no competing interests.

Additional information

Supplementary information The online version contains supplementary material available at https://doi.org/10.1038/s41524-024-01416-1.

Correspondence and requests for materials should be addressed to Jackson L. Ross.